

Modeling of Rolling Texture Development in a Ferritic Chromium Steel

L.S. TÓTH, A. MOLINARI, and D. RAABE

The development of crystallographic texture during rolling of a ferritic chromium steel containing 11 pct Cr was examined experimentally as well as by polycrystal modeling at large strains (up to 90 pct thickness reduction). The initial shape of the grains was very much elongated in the direction of rolling. A strong rolling direction (RD) fiber ($\langle 110 \rangle$ parallel to the rolling direction) has been observed at large strains in the experiment. The Taylor viscoplastic model, the relaxed-constraints pancake model, and the self-consistent viscoplastic approach were employed to simulate the texture development. Strain hardening was accounted for by microscopic hardening laws, for which the parameters were obtained from uniaxial tensile tests. It has been found that among the three models considered, the self-consistent viscoplastic model (the version tuned to finite-element results) yielded the best agreement with the experimentally observed texture evolution. Strong effects of grain shape and hardening have been found. The pancake model was also able to reproduce the main characteristics of the texture because of the flattened initial grain shape.

I. INTRODUCTION

MODELING of texture development has great technological importance, as plastic deformation usually induces strong anisotropies in polycrystalline metals, leading to directional dependencies of the physical properties. The behavior of an individual crystal, however, depends on its interaction with its surroundings, which is difficult to account for. Early models (Sachs^[1] and Taylor^[2]) assumed stress and strain homogeneity, respectively. However, these idealized conditions were not perfectly verified by measurements or simulation results. It was recognized that grain-shape effects can be important, and were first taken into account by the relaxation of some stress components (relaxed-constraints model^[3-6]). These relaxations, however, can only be justified when the grain shapes are far from equiaxed, *i.e.*, are normally at very large strains (except when they are elongated already at the beginning of deformation, a case that will be studied in the present work).

An important step was taken with the introduction of the self-consistent models,^[7-10] which consider a grain as an inclusion embedded in the polycrystal. A grain's surroundings is a homogeneous equivalent medium (HEM) in these models, which is defined by the average physical properties of all grains. This approach can naturally account for the shape and its evolution during deformation. It introduces an interaction law between a grain and the polycrystal, for which several approaches were proposed, namely, secant,^[8] tangent,^[9] and finite-element-tuned^[10] models. Among these, the one that has been calibrated with the help of some finite-element calculations will be employed in the present study.^[10] This modified self-consistent model has already been successfully tested for torsion and rolling.^[11,12] For completeness and in order to estimate the performance of

the self-consistent model, the classical Taylor and relaxed-constraint approaches will also be considered. All models employed in the present work use the well-known viscoplastic power law for crystallographic slip, incorporating microscopic strain hardening of the slip systems.

The cold-rolling textures of a ferritic chromium sheet steel containing 11 pct Cr are studied in the present work. Before cold rolling, it contained already very elongated grains in its middle section, where the textures were measured and also simulated. Important effects of grain shape and hardening were found, which have been studied by the Taylor, the relaxed-constraints pancake, and the self-consistent viscoplastic models.

II. EXPERIMENTAL

A. Material and Rolling Conditions

Table I shows the chemical composition of the ferritic stainless steel under investigation. The material was continuously cast and unidirectionally hot rolled, passing 7 four-high stands, to a final thickness of 3 mm. The first pass was carried out within the temperature range of 1400 to 1460 K, and the last pass within the range of 1200 to 1300 K. After hot rolling, the steel was annealed at 1300 K. Cold rolling was carried out to a final reduction of $\epsilon = 90$ pct ($\epsilon =$ the technical thickness reduction, $\Delta d/d_0$). The samples were rotated 180 deg about the transverse direction after each pass. Since homogeneous deformation is primarily determined by the ratio of contact length, l_c , to sheet thickness, d , a ratio of $1 < (l_c/d) < 3$ was obtained during cold rolling.

According to the metallurgical observations, the grain shapes in the center layer of the hot band are elongated substantially in the direction of rolling, with aspect ratios of about 7:2:1, in the sense of rolling direction (RD), transverse direction (TD), and normal direction (ND), respectively. This situation, which is attributable to substantial recovery during hot rolling, offers an excellent opportunity to examine the effect of grain shape on the development of the texture.

L.S. TÓTH and A. MOLINARI, Professors, are with the Laboratoire de Mécanique et Physique des Matériaux, Université de Metz, 57045 Metz, France. D. RAABE, Private Dozent, is with the Institute für Metallkunde und Metallphysik, 52056 Aachen, Germany.

Manuscript submitted January 8, 1997.

Table I. Chemical Composition of the Ferritic Stainless Steel (Balance Fe), Pct = Mass Percent

Cr	C	N	Ti	Nb
10.5 pct	0.01 pct	0.02 pct	0.11 pct	0.32 pct

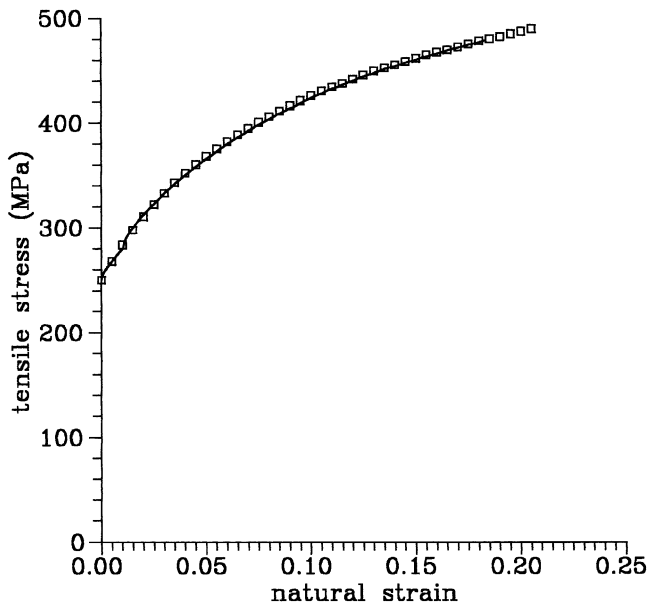


Fig. 1—Measured (continuous line) and fitted (squares) true stress–true strain curves for tension of the chromium alloy at 0 deg RD.

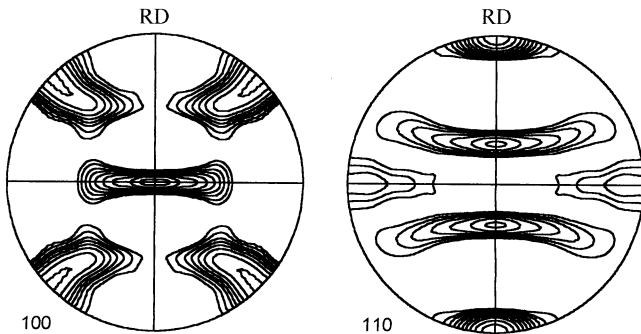


Fig. 2—{100} and {110} pole figures showing the initial experimental textures in the Fe 11 pct Cr sheet in the center layer. Intensity levels: 1.0, 1.3, 1.6, 2.0, 2.5, 3.2, and 4.0.

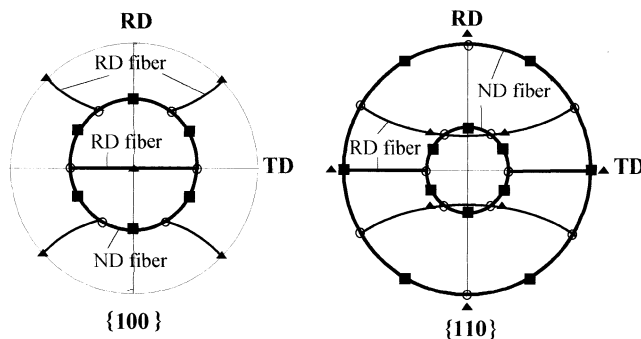


Fig. 3—Key figures for the location of the ideal orientations of the bcc rolling textures. Legend: ○ (111)[110], ■ (111)[121], and ▲ (001)[110].

B. Tensile Tests

Figure 1 shows the measured hardening curve in the tensile test (at a strain rate $\dot{\epsilon}$ of $1.5 \cdot 10^{-4} \text{ s}^{-1}$) for samples that were cut parallel to the rolling direction. The measured R value was 1.44. The strain-rate sensitivity index ($m = d \ln \sigma / d \ln \dot{\epsilon}$, where σ is the flow stress) was also measured in the tensile tests by varying the strain rate, and was found to be $m = 0.02$ at room temperature.

C. Texture Measurements and Experimental Results

The textures were examined by measuring four pole figures {110}, {200}, {112}, and {103} in the range of the pole distance angle α from 5 to 85 deg using $MO_{K\alpha}$ radiation in the back-reflection mode.^[13] In order to remove a layer of 20 μm , the samples were etched in a solution of 50-mL H_2O and 10-mL HF prior to measurement.

The orientation distribution function (ODF) was derived using the iterative series expansion method.^[14] This approach makes use of two assumptions, which yield considerable improvement in pole figure inversion, as compared to conventional Fourier methods. The first ingredient, referred to as the non-negativity condition, implies that negative pole densities are physically senseless. The second condition is the so-called “phon concept,” where the term “phon” describes an isotropic background component. This condition increases the non-negativity constraint in such a manner that the minimum pole densities of the unmeasured recalculated pole figures are not only set equal to zero, but also to the pole density of the phon component. To reduce truncation errors, a series expansion degree of $l_{\text{max}} = 34$ was used. In order to provide a convenient presentation, the experimental data are presented in the form of pole figures, which were recalculated from the ODF.

Ferritic stainless steels tend to develop characteristic fiber textures, such as the so-called α -RD fiber, $\{hkl\} \langle 110 \rangle$ ($\{hkl\}$ normal to the sheet surface, $\langle uvw \rangle$ parallel to RD) and the γ -ND fiber, $\{111\} \langle uvw \rangle$. As is well known from previous investigations,^[15] the texture and microstructure of ferritic stainless steels are very inhomogeneous throughout the sheet thickness. Thus, in the present investigation, the textures in the center layer are examined.

As a result of hot-band rolling, the sheet has a strong initial texture, which is shown in Figure 2 in the form of {100} and {110} pole figures. It contains a strong but not even distribution of the RD fiber (*i.e.*, $\langle 110 \rangle$ parallel to the rolling direction, see the key figure, Figure 3).

The textures measured at 35, 80, and 90 pct rolling reductions are displayed in Figure 4. They show a progressive evolution of the RD fiber leading to a more uniform distribution along the fiber.

D. Discretization of the Experimental Initial Textures

For the purpose of texture simulations, a discrete set of grain orientations is necessary. This was produced from the initial texture by the technique of Wagner.^[16] In this approach, the number of grains (texture components) is linearly related to the respective orientation density in Euler space.

This *initial* distribution was symmetrized for the case of the self-consistent simulations with respect to RD, TD, and

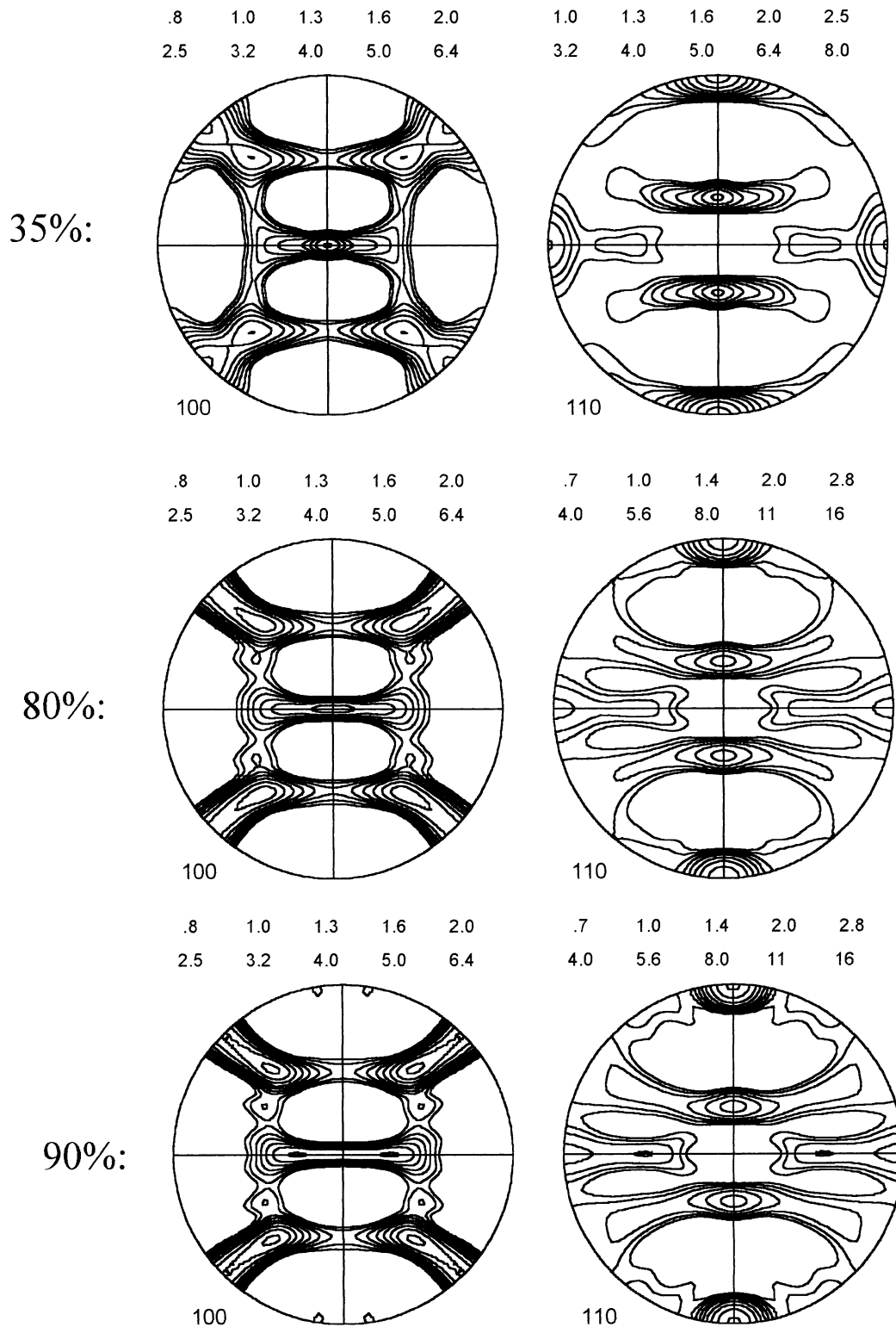


Fig. 4—Textures measured at increasing rolling reductions in the sheet center layer. Number lists above each pole figure show corresponding isolevels.

ND planes, assuring the orthotropy of the texture. In this way, a population of 3100 grains was used in the tensile-test simulations, and 2800 in the case of rolling, both representing very well the experimental initial texture.

The condition of orthotropic distribution of grain orientations is necessary only in the use of the self-consistent model for rolling. The reason is that in the real sample, the

distribution is orthotropic during rolling, which implies that the HEM, which is made of all grains in the model texture, has to possess the same property.

It has to be noted that the symmetry requirement is not necessary in a classical Taylor or relaxed-constraints calculation, as the behavior of individual grains does not depend on the other crystals. Moreover, the behavior of those

grains that are in symmetrical positions with respect to the RD, TD, and ND planes is exactly the same under both Taylor and relaxed-constraints conditions. Thus, a symmetrization of the initial distribution was not applied for the cases of Taylor and relaxed-constraints calculations. This means that 4 times less individual orientations are sufficient in those cases. For the purpose of presenting pole figures, the nonsymmetric orientation distribution has to be symmetrized *after* the simulation.

III. MAIN ELEMENTS OF THE SELF-CONSISTENT MODEL

In the present work, the self-consistent viscoplastic model originally proposed by Molinari *et al.*^[9] is employed in a slightly modified form, namely, the version that was tuned to finite-element results by Molinari and Tóth.^[10] This modification consists of the introduction of a calibration parameter α in the interaction law that describes the interaction between a grain and the matrix, as follows:

$$s^g - S = \alpha \left[\left(\Gamma^{sgg} \right)^{-1} + A^s \right] [d^g - D] \quad [1]$$

Here, d^g and s^g are the strain rate and the deviatoric stress in the grain, respectively, and D and S are the same quantities at the macroscopic level; *i.e.*, for the matrix (the equivalent homogeneous medium, consisting of all grains). The term A^s is the macroscopic secant modulus defined by $S = A^s D$, and the tensor Γ^{sgg} accounts for the shape of the grain during deformation and is calculated with the help of the Green functions associated with the modulus A^s . For more details, see the original articles of Molinari *et al.*^[9,10] In the present work, the isotropic version of the self-consistent model was employed based on a previous calibration of the interaction law, Eq. [1]. The tuning was carried out by introducing the scalar parameter α in Eq. [1], which was determined by comparing the predictions of the average properties obtained from the present self-consistent model to finite-element results. The latter were calculated for a spherical inclusion embedded into an infinite matrix, in an earlier work carried out by Gilormini and Germain.^[17] For this special case of a spherical inclusion and isotropy, a simple relation was found between the parameter α and the strain-rate sensitivity index m , as follows:^[10]

$$\alpha = 1 - 0.4(m - 1)^2 \quad [2]$$

Since for the present material m is very low (0.02), α could be taken as 0.6. This value of α corresponds to spherical inclusions, whereas in the present material, the grain shape is already very much ellipsoidal, prior to cold rolling. Therefore, α does not necessarily have to be the same as for the spherical case. For this reason, a wide range of the α parameter will be examined in the present work, and the resulting textures will be compared to the experimental ones. In fact, varying the α parameter corresponds to different models proposed in the past, as follows:

- $\alpha = 0$: static model,
- $\alpha = m$: tangent model,^[9]
- $\alpha = 1$: secant model, and
- $\alpha = \infty$: Taylor model.^[2]

IV. MICROSCOPIC HARDENING

In rate-sensitive slip, the usual power law is commonly used to relate the slip rate $\dot{\gamma}^s$ to the stress level τ in a slip system identified by the index s , as follows:^[18]

$$\dot{\gamma}^s = \dot{\gamma}_0^s \frac{\tau^s}{\tau_0^s} \left\| \frac{\tau^s}{\tau_0^s} \right\|^{m-1} \quad [3]$$

Self and latent hardening can be readily accounted for by a suitable evolution of the reference τ_0^s values in the constitutive law of Eq. [3].^[19,20] In the present work, the approach of Kalidindi *et al.*^[20] has been employed for this purpose, which uses the following hardening law:

$$\dot{\tau}_0^i = \sum_j H^{ij} |\dot{\gamma}^j| \quad i, j = 1 \dots n \quad [4]$$

$$H^{ij} = q^{ij} h_0 \left(1 - \frac{\tau_0^i}{\tau_{sat}} \right)^a \quad [5]$$

where n is the total number of slip (and twinning) systems in Eq. [4], and H^{ij} is a $(n \times n)$ hardening matrix. The latter is introduced to account for the interactions between slip systems. This interaction is twofold. First, it contains a q^{ij} matrix, which expresses the *geometrical* relation between the slip systems. Second, the interaction is governed by a power function that is defined by the exponent a , the parameter h_0 , and the saturation value of the reference stress, τ_{sat} . As for the geometrical factor q^{ij} , the proposition of Zhou *et al.*^[21] has been adopted, which distinguishes the following four cases: (1) coplanar slip ($q^{ij} = q_1$); (2) collinear slip ($q^{ij} = q_2$); (3) systems with perpendicular glide ($q^{ij} = q_3$); and (4) all others ($q^{ij} = q_4$).

According to the aforementioned definitions, the parameters required to formulate the microscopic hardening law are the following: $\dot{\gamma}_0^s$, τ_0^s , a , h_0 , τ_{sat} , q_1 , q_2 , q_3 , and q_4 . They may seem to be quite numerous; however, for their identification, several physical ideas of dislocation dynamics can be used. For the derivation of the q_1 , q_2 , q_3 , and q_4 parameters, see References 21 and 22. Since the chosen values of the $\dot{\gamma}_0^s$ parameters do not influence the texture development, they can be assumed equal. The initial values of the τ_0^s parameters can also be taken to be equal within one slip-system family if the material is well annealed and stress released prior to deformation. These values, however, usually vary from one slip-system family to another. The relative strengths of the different slip-system families can be determined from single-crystal experiments, or by special techniques; see the recently proposed method of Tóth and Serghat.^[23] Another possibility is to obtain them by modeling measured hardening curves. This technique is also proposed in the present study for the remaining hardening coefficients, a , h_0 , and τ_{sat} .

As in earlier simulations,^[24,25] three families of slip systems were considered in the simulations: the $\{110\}$, the $\{112\}$, and the $\{123\}$ slip planes, all with the well-known $\langle 111 \rangle$ slip directions. They represent 48 systems (12 $\{110\}\langle 111 \rangle$, 12 $\{112\}\langle 111 \rangle$, and 24 $\{123\}\langle 111 \rangle$). For the initial strengths of these systems, the very same values were employed within one family; however, preference was given for the $\{112\}\langle 111 \rangle$ slip by prescribing a relative strength of 90 pct of those corresponding to the other two families, which were taken to be equal. The relatively eas-

Table II. Values of the Microscopic Hardening Coefficients Derived from the Fitting of the Experimental Tensile Test Curve Shown in Figure 1 for the Self-Consistent Model with $\alpha = 0.6$ and $q_1 = 1$, $q_2 = 1$, $q_3 = 1.4$, and $q_4 = 1.2$

a	h_0 (MPa)	τ_{sat} (MPa)	$\tau_0^{\{110\}}$ (MPa)	$\tau_0^{\{112\}}$ (MPa)	$\tau_0^{\{123\}}$ (MPa)
2.08	1700	252	117.9	106.1	117.9

iest slip on $\{112\}$ planes has been suggested in earlier studies.^[12,26,27]

It is obvious that the values of the microscopic hardening coefficients are model dependent. Therefore, for each model, they were determined from the tensile test, by reproducing the experimental curve nearly perfectly by the polycrystal simulations. In this fitting procedure of the hardening parameters, first the values of the initial reference stresses were identified by reproducing the yield stress of the material. Subsequently, incremental iterative types of simulations were carried out by varying the hardening parameters (a , h_0 , and τ_{sat}) until a perfect agreement was obtained between the predicted and the measured tensile-test curves. For the rate-sensitivity exponent in the constitutive law, Eq. [3], the measured macroscopic m value was used ($m = 0.02$). Concerning the prescribed deformation of the polycrystal, the velocity gradient corresponding to a strain rate of 1 s^{-1} was employed in the rolling direction, whereas the other two normal components were imposed with the help of the measured R value ($R = 1.44$). The hydrostatic component was obtained using the condition of zero normal stress in the ND of the tensile model specimen. Finally, the tensile stress curve was plotted and compared to the measured one.

The aforementioned fitting procedure led to the values displayed in Table II for the hardening coefficients for the self-consistent model, with $\alpha = 0.6$ and with $q_1 = 1$, $q_2 = 1$, $q_3 = 1.4$, and $q_4 = 1.2$. In order to show the quality of fitting, the simulated curve obtained for this case is also plotted in Figure 1.

V. PREDICTED TEXTURES

A. Textures Predicted by the Self-Consistent Model

The discrete distribution generated from the starting texture (2800 grains in orthotropic symmetry) together with the microscopic hardening parameter was used to model the texture development with the help of the self-consistent model. Different α values were used in the interaction law (Eq. [1]) so that the dependence of the predicted textures on α could be examined. This dependence was investigated because the self-consistent viscoplastic model was calibrated for spherical grains, whereas in the present case, the grains are already strongly elliptical at the beginning of rolling.

Since the grains were flattened at zero strain, with aspect ratios of 7:2:1 (with respect to the RD, TD, and ND, respectively), the initial shapes of the grains in the simulations were taken to be elliptical, for each grain with the same form. They were also updated during rolling, leading to extremely elongated grains at large strains.

The parameter α was taken to be 0.2, 0.6, 2, 10, 100,

and ∞ and the textures have been derived with the self-consistent model (for $\alpha = \infty$, the Taylor viscoplastic model was used). In order to save space, the resulting pole figures are presented only at the largest strain, at 90 pct rolling reduction (Figure 5).

Detailed comparisons of the predicted textures with the measured ones (compare Figure 5 with Figures 4) permit the conclusion that the textures obtained for $\alpha = 0.6$ are in best agreement with the measurement. For the smallest α value, variations in the pole figures can be seen, which show a deterioration of the predictions. A similar conclusion can be drawn from the pole figures obtained for $\alpha = 2$, 10, and 100 in Figure 5, which shows the gradual strengthening of the $(112)[110]$ orientation, which is in disagreement with the experiments. In fact, the strengthening of this component shows that the conditions tend toward the Taylor case, see Figure 5 for $\alpha = \infty$.

From the results supplied by the self-consistent model, we can conclude that this approach is able to reproduce the experimental texture with a good precision. Concerning the dependence of the results on the tuning parameter α , it is not too strong in the expected range of this parameter (*i.e.*, between $\alpha = 0.2$ and 2.0). Nevertheless, the best result corresponds to $\alpha = 0.6$, which is the value obtained from the previous tuning of the self-consistent model.^[10] Therefore, further results obtained with the self-consistent model will be examined for the case of $\alpha = 0.6$ in the present article.

B. Effects of Grain Shape Predicted by the Self-Consistent Model

Since the grain shapes were particularly flattened at the beginning of rolling, they may cause important variations in the development of the texture. In order to check the effect of the initial-grain shape on the predicted textures, another simulation was performed with the self-consistent model, namely, with the initial grain shapes equiaxed at zero strain. (Their form development during rolling, however, was taken into account in the simulation.) The textures obtained from this simulation are presented in Figure 6 for a rolling reduction of 90 pct and with an α parameter of 0.6.

As can be seen from Figure 6, the simulated texture deviates considerably from the experimental one (compare with Figure 4) when the initial shape is considered equiaxed. The main difference is the loss of the fiber characteristic in the texture. Instead, the $\{111\}\langle 1\bar{1}0 \rangle$ texture component seems to be excessively strong. The shape of initially spherical grains becomes strongly flattened because of the large strain they experience, up to the aspect ratios of 10:1:0.1 in the RD, TD, and ND, respectively. However, when the real initial grain shape is considered, the final aspect ratios after 90 pct rolling reduction amount to 35:1:0.05. In this context, one should note that the individual shape development of the grains is different from each other in self-consistent modeling, although the average shape follows the imposed strain of the sample. As can be seen from these aspect ratios, the final grain shape depends strongly on the initial one. It can be concluded from the results obtained in this section, that the initial shape has a substantial influence on the texture development at large strains.

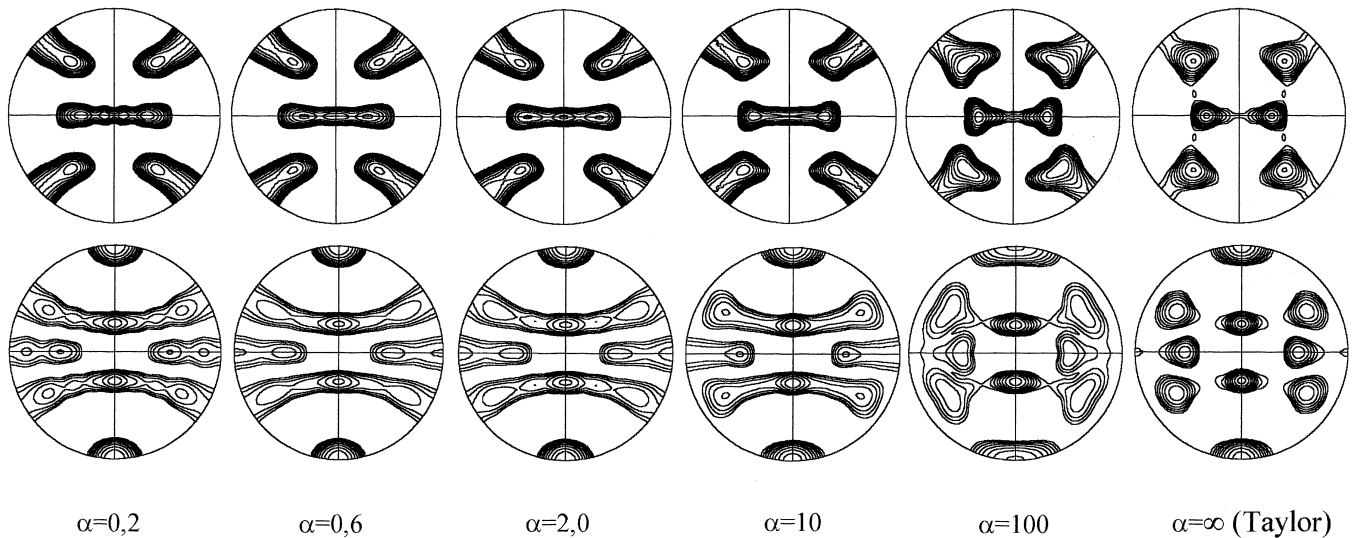


Fig. 5—Simulated pole figures obtained by the self-consistent model (top line: {100}, bottom line: {110}) for a rolling reduction of 90 pct at different values of the α parameter. (Isovalues for the {100} pole figures: 0.8, 1.0, 1.3, 1.6, 2.0, 2.5, 3.2, 4.0, 5.0, and 6.4, except for $\alpha = \infty$, where they are 0.7, 1.0, 1.4, 2.0, 2.8, 4.0, 5.6, 8.0, and 11.0. Isovalues for the {110} pole figures: 0.7, 1.0, 1.4, 2.0, 2.8, 4.0, 5.6, 8.0, and 11.0, except for $\alpha = 100$, where they are 1.0, 1.3, 1.6, 2.0, 2.5, 3.2, 4.0, 5.0, 6.4, and 8.0.)

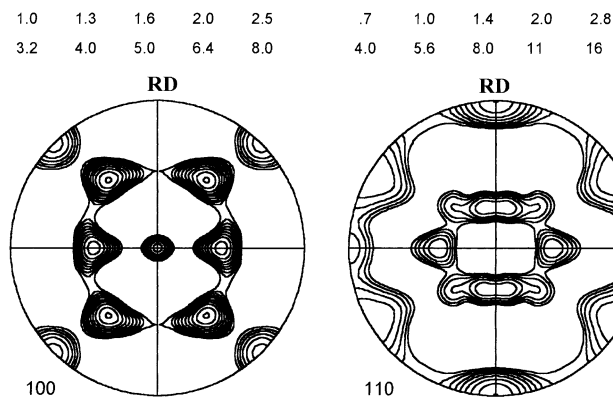


Fig. 6—Predicted textures for 90 pct rolling reduction obtained with the self-consistent model for initially *spherical* grain shape. Numbers above the figure indicate isovels.

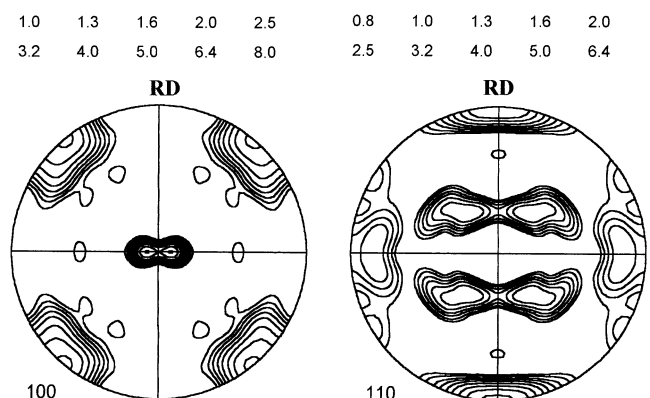


Fig. 7—Predicted textures for 90 pct rolling reduction obtained with the self-consistent model *without* hardening but using initial shape and its development during deformation. Numbers above the figure indicate isovels.

C. Effect of Hardening on Texture Development in Self-Consistent Modeling

Hardening is frequently neglected in polycrystal modeling when only the texture development is examined. This can be accepted in the case of isotropic hardening and Taylor modeling. However, hardening can be important in the self-consistent case because of the interaction of individual grains with the HEM. In order to demonstrate this effect, a simulation has been carried out where hardening was completely neglected. In this case, the initial values of the reference stresses were used throughout the deformation. However, the initial shape and the subsequent shape changes during deformation were considered. The resulting textures obtained in this way are displayed in Figure 7, after 90 pct rolling reduction for an α parameter of 0.6. One can see from this figure that without hardening, this particular simulation does not reproduce all the ideal components observed in the experiment.

D. Some Results Obtained at the Microscopic Scale in Self-Consistent Modeling

1. Grain deformation

An important characteristic of the self-consistent model is that the deformation of individual grains generally differs from the imposed macroscopic one. It is interesting to study this aspect of the deformation process at the beginning of deformation, as well as at large strains. For this purpose, the average standard deviation of the strain rate of grains with respect to the macroscopic one is calculated and displayed in the following matrices for a strain rate of $D_{11} = 1.0 \text{ s}^{-1}$:

$$\text{at 0 pct rolling: } \begin{bmatrix} 0.15 & 0.15 & 0.42 \\ 0.15 & 0.15 & 0.31 \\ 0.42 & 0.31 & 0.15 \end{bmatrix}$$

Table III. Relative Activity of the Slip-System Families, Number of Active Slip Systems, and the Slip Localization Parameter at the Beginning of Deformation and at Large Strain According to the Self-Consistent Model

	0 Pct Rolling	90 Pct Rolling
Slip family $\{110\}\langle 111\rangle$	44.5 pct	47.5 pct
Slip family $\{112\}\langle 111\rangle$	51.7 pct	18.0 pct
Slip family $\{123\}\langle 111\rangle$	3.7 pct	34.5 pct
Number of active slip systems	4.13	5.55
Slip localization in the most active slip system	59 pct	38 pct

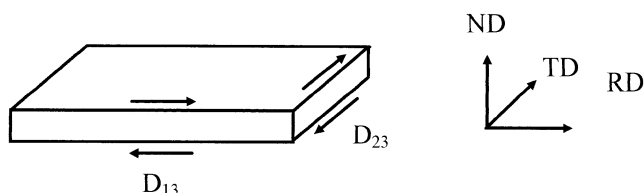


Fig. 8—Strain rate components, which can be relaxed in the pancake model when the grain shape is very much elongated.

$$\text{at 90 pct rolling: } \begin{bmatrix} 0.005 & 0.001 & 0.29 \\ 0.001 & 0.005 & 0.30 \\ 0.29 & 0.30 & 0.005 \end{bmatrix}$$

As can be seen from the above-average strain-rate deviation matrices, the average deformation of the grains is quite different from that of the whole sample. For each strain-rate component, there occurs a deviation of at least 15 pct. This deviation seems to be larger for two components, D_{13} and D_{23} , as compared to the other ones. As it will be studied in Section 2, these are the components to be relaxed in the pancake model. At large strains, the situation changes significantly. The deviation of the strain components of individual grains from the macroscopic one decreases to nearly zero concerning the normal components D_{11} , D_{22} , and D_{33} , and one shear component, D_{12} . The pancake-type strain components, however, still deviate from the macroscopic one by about 30 pct.

2. Slip-system activity

Three slip-system families were considered to be available in the present material and also in the simulations, namely, $\{110\}\langle 111\rangle$, $\{112\}\langle 111\rangle$, and $\{123\}\langle 111\rangle$. It was assumed that the easiest one is the $\{112\}\langle 111\rangle$ family, at least at the beginning of deformation, with a relative critical resolved shear stress (CRSS) value of 0.9, with respect to the other two families, where the CRSS's were set equal to each other (Table II). As a consequence of the different initial strengths of the slip systems, their activity varies from one family to the other and also as a function of strain. The relative activity of a slip-system family can be readily calculated by summing up the absolute values of all slip rates that take place in the corresponding slip systems of the same family, and divide that by the sum of the total slip rate in a grain. An average value can also be obtained for the entire polycrystal by averaging the single-crystal slip-family activity values on the whole polycrystal. Some results obtained in this way are displayed in Table III.

At the beginning of deformation, the $\{112\}\langle 111\rangle$ family has the lowest critical stress. Hence, it is expected that this family would be the most active one. This is in fact the

case, as can be seen from the values in Table III. As a result of the present nonisotropic hardening, however, the situation changes. The activity of the $\{112\}\langle 111\rangle$ family decreases considerably at large strains, whereas the relative activity of the other two types of systems increases (Table III).

The number of active slip systems was also calculated in the present simulations. A slip system was considered to be active if at least 5 pct of the total slip in a grain is concentrated on it. Table III displays the average number of active slip systems of the polycrystal. As can be seen from this table, the number of active slip systems increases from 4.13 to 5.55 at large strain, indicating that multiple slip takes place already at the very beginning of plastic deformation. The aforementioned definition for the number of active slip systems, however, does not give any information on the slip pattern; *i.e.*, on the spatial distribution of shear among the operating slip systems. Indeed, in order to achieve a better characterization of the slip-system activity, another quantity was also calculated and displayed in Table III, the average percentage of the shear corresponding to the most active system with respect to the total slip in a grain. This parameter was calculated in each grain, and was also averaged at the polycrystal level. At the beginning of straining, this slip localization parameter amounts to almost 60 pct, and thus only 30 pct of the total slip is distributed among the other active slip systems. This situation, in fact, is not too far from the single slip case, the Sachs model. At large strains, however, the slip localization factor is only 38 pct (Table III), which clearly indicates that there is a multiple slip situation. However, this case does not reflect a classical Taylor-type situation as the grain strain deviates considerably from the macroscopic one for two shear components. The tendency of developing multiple slip is understandable, when considering the fact that at large strains, all grains approach the ideal positions where there is multiple slip. It was shown in a previous work that in rolling, the minimum number of active slip systems is actually four for an ideal orientation.^[28]

VI. RESULTS OBTAINED BY THE PANCAKE MODEL

In the pancake model, it is assumed that such shear-strain components that produce incompatibilities in the narrow lateral grain boundaries can be tolerated. This assumption implies zero stresses for the corresponding shear components. These components are displayed in Figure 8. Since the grain shape in the present case is already very elongated at the beginning of cold rolling, it can be expected that the conditions of the pancake model are nearly fulfilled; *i.e.*, this model should be able to reproduce the experimental textures.

The development of the texture was modeled with the pancake model using the same *relative* initial CRSS values for the three slip-system families and the same microscopic hardening law described previously, employing the hardening parameters obtained from the fitting of the tensile-test experiment by the pancake model. The texture obtained at 90 pct rolling reduction is displayed in Figure 9. It can be seen from the comparison of this figure with the experimental texture (Figure 4) that the main characteristics of the texture are reproduced. In fact, the pancake texture is

0.8	1.0	1.3	1.6	2.0	0.7	1.0	1.4	2.0	2.8
2.5	3.2	4.0	5.0	6.4	4.0	5.6	8.0	11	16

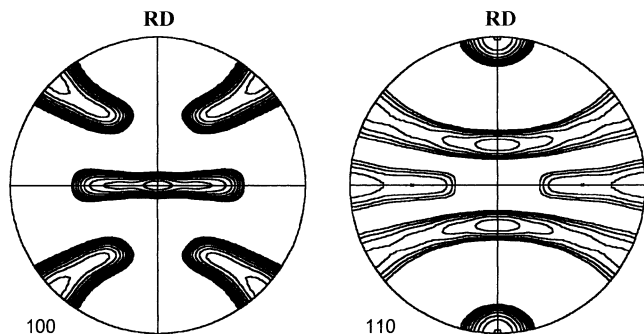


Fig. 9—Simulation result obtained by the relaxed constraints pancake viscoplastic model at 90 pct rolling reduction. Numbers above the figure indicate isolevels.

.7	1.0	1.4	2.0	2.8	.7	1.0	1.4	2.0	2.8
4.0	5.6	8.0	11	16	4.0	5.6	8.0	11	16

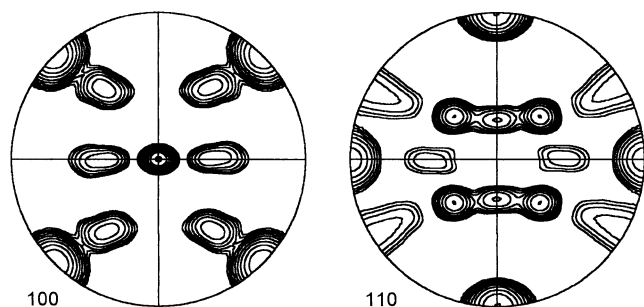


Fig. 10—Simulation result obtained by the relaxed constraints pancake viscoplastic model at 90 pct rolling reduction *without* hardening. Numbers above the figure indicate isolevels.

also similar to the one predicted by the self-consistent model for $\alpha = 0.6$ (Figure 5). Close inspection reveals, however, that the pancake model predicts the $\{001\} \langle 110 \rangle$ component to be the strongest along the RD fiber, whereas in the experiment, and also in the self-consistent case, the maximum is located at the $\{111\} \langle 110 \rangle$ orientation. Thus, the self-consistent model approximates the experimentally observed texture better than the pancake model.

The effect of hardening in the case of the pancake model is similar to the one in self-consistent modeling. When microscopic hardening is neglected, the obtained texture is in poor agreement with the experimental one. This situation is illustrated in Figure 10, where the pole figures of the texture are shown after 90 pct rolling reduction without using hardening. The main deviation from the experimental texture is the absence of the continuous fibers; *i.e.*, only some ideal components are strengthened along the fibers.

The effect of microscopic hardening on texture development was also studied earlier by Kocks *et al.*^[29] in rolling, compression, and tension, with gradual relaxed-constraints conditions and using a forest model of latent hardening. They found little effect of hardening on the development of the texture, except for compression. Their approach, however, is based on some theoretical estimates of the latent hardening coefficients, whereas in the present work they were obtained from a fitting procedure of the hardening curves of tensile tests. The strong hardening effects observed in the present study may be due to the previously

described precise calibration technique of the hardening coefficients, which may give more realistic values.

VII. CONCLUSIONS

In this work, the texture development was studied in a ferritic chromium steel by rolling experiments as well as by theoretical modeling. An interesting feature of the microstructure was that the grain shape was already very much elongated prior to cold rolling in the center region of the sheets. The self-consistent model, the relaxed-constraints pancake, and the full-constraints Taylor approaches were applied for the prediction of the development of crystallographic texture, with special regard to the effect of grain shape, as well as to microscopic hardening. From the results obtained, the following conclusions can be drawn.

1. The finite-element tuned self-consistent model reproduces precisely the experimental texture development when grain-shape evolution and microscopic hardening are both included.
2. When either hardening or the grain-shape influence are dropped in the model, the experimental textures are not well reproduced. Therefore, both are decisive elements of the self-consistent approach.
3. The relaxed-constraints pancake model leads to textures that approach the experiments relatively well because of the elongated initial grain shape. The relative experimental pole densities of the components, however, are not well predicted. The decisive effect of hardening on the development of the texture was also verified in the pancake model.
4. The self-consistent model justifies the relative applicability of the pancake model, as exactly the same shear components are relaxed in the self-consistent case at large strains as in the pancake model. The advantage of the application of the self-consistent model is that it is able to account for the grain shapes and applies the "relaxation" of certain components in an automatic way.
5. Nearly 60 pct of the total slip is, in average, concentrated in the most active slip system at the beginning of rolling, suggesting in this way a slip pattern that is not too far from single slip. This situation changes at large strains, where multiple slip applies.

REFERENCES

1. G. Sachs: *Z. Ver. Dtsch. Ing.*, 1928, vol. 72, p. 734.
2. G.I. Taylor: *J. Inst. Met.*, 1938, vol. 62, pp. 307-24.
3. H. Honneff and H. Mecking: *Proc. ICOTOM5*, Aachen, 1978, G. Gottstein and K. Lücke, eds., Springer-Verlag, Berlin, 1978, vol. 1, pp. 265-76.
4. U.F. Kocks and H. Chandra: *Acta Metall.*, 1982, pp. 695-709.
5. P. Van Houtte: *Proc. ICOTOM6*, S. Nagashima, ed., ISIJ, Tokyo, 1981, pp. 428-37.
6. G.R. Canova: Ph.D. Thesis, McGill University, Montreal, 1982.
7. R. Hill: *J. Mech. Phys. Sol.*, 1967, vol. 15, pp. 79-95.
8. M. Berveiller and A. Zaoui: *Res. Mech. Lett.*, 1981, vol. 1, p. 119.
9. A. Molinari, G.R. Canova, and S. Ahzi: *Acta Metall.*, 1987, vol. 35, pp. 2983-94.
10. A. Molinari and L.S. Tóth: *Acta Metall. Mater.*, 1994, vol. 42, pp. 2453-58.
11. L.S. Tóth and A. Molinari: *Acta Metall. Mater.*, 1994, vol. 42, pp. 2459-66.
12. S. Mercier, L.S. Tóth, and A. Molinari: *Textures and Microstructures*, 1995, vol. 25, pp. 45-61.

13. L.G. Schulz: *J. Appl. Phys.*, 1949, vol. 20, pp. 1030-34.
14. M. Dahms and H.J. Bunge: *J. Appl. Cryst.*, 1989, vol. 22, pp. 439-47.
15. D. Raabe and K. Lücke: *Mater. Sci. Technol.*, 1993, vol. 9, pp. 302-12.
16. P. Wagner: Ph.D. Dissertation, Rheinisch-Westfälische Technische Hochschule Aachen, Aachen, 1995.
17. P. Gilormini and Y. Germain: *Int. J. Solids Struct.*, 1987, vol. 23, pp. 413-37.
18. J.W. Hutchinson: *Proc. R. Soc. London*, 1976, vol. A348, pp. 101-27.
19. P. Franciosi: *Acta Metall.*, 1985, vol. 33, pp. 1601-12.
20. S.R. Kalidindi, C.A. Bronkhorst, and L. Anand: *J. Mech. Phys. Solids*, 1992, vol. 40, p. 537.
21. Y. Zhou, K.W. Neale, and L.S. Tóth: *Int. J. Plasticity*, 1993, vol. 9, pp. 961-78.
22. L.S. Tóth: *Proc. ICOTOM11*, International Academic Publishers, eds. Z. Liang, L. Zuo, and Y. Chu, Xi'an, China, 1996, pp. 347-55.
23. L.S. Tóth and M. Serghat: *Textures Microstr.*, 1996, vols. 26-27, pp. 221-29.
24. D. Raabe: *Mater. Sci. Eng.*, 1995, vol. A197, pp. 31-37.
25. D. Raabe: *Mater. Sci. Technol.*, 1995, vol. 11, pp. 455-60.
26. D. Daniel and J.J. Jonas: *Metall. Trans. A*, 1990, vol. 21A, pp. 331-43.
27. L.S. Tóth, J.J. Jonas, D. Daniel, and R.K. Ray: *Metall. Trans. A*, 1990, vol. 21A, pp. 2985-3000.
28. L.S. Tóth, J.J. Jonas, and K.W. Neale: *Proc. R. Soc. London*, 1990, vol. A427, pp. 201-19.
29. U.F. Kocks, P. Franciosi, and M. Kawai: *Textures Microstr.*, 1991, vols. 14-18, pp. 1103-14.